

Myotonic dystrophy RNA toxicity alters morphology, adhesion and migration of mouse and human astrocytes

Diana Dincă

Inserm

Anchel González-Barriga

Inserm <https://orcid.org/0000-0001-7072-5494>

Geraldine Sicot

Inserm UMR1163, Imagine Insitute

Louison Lallemant

Inserm

Laure-Elise Pillet

College de France

Noémie Cresto

College de France

Sandra Braz

Inserm

Helene Polveche

CECS, I-Stem, Corbeil-Essonnes, 91100, France

Aline Huguet

Inserm U781

Cuauhtli N. Azotla-Vilchis

National Rehabilitation Institute <https://orcid.org/0000-0002-3478-4427>

Luis Agonizantes-Juárez

National Rehabilitation Institute

Julie Tahraoui-Bories

INSERM/UEVE 861

Cecile Martinat

Inserm

Oscar Hernández-Hernández

National Rehabilitation Institute <https://orcid.org/0000-0001-6388-2459>

Didier Auboeuf

Inserm <https://orcid.org/0000-0002-3757-0002>

Nathalie Rouach

Collège de France <https://orcid.org/0000-0002-5574-888X>

Cyril F Bourgeois

INSERM <https://orcid.org/0000-0002-0756-5501>

Genevieve Gourdon

Inserm UMR1163, Imagine Insitute

Mário Gomes-Pereira (✉ mario.pereira@inserm.fr)

Inserm <https://orcid.org/0000-0002-3533-0873>

Article

Keywords: myotonic dystrophy type 1, RNA, astrocytes

Posted Date: October 19th, 2021

DOI: <https://doi.org/10.21203/rs.3.rs-137333/v1>

License:  This work is licensed under a Creative Commons Attribution 4.0 International License.

[Read Full License](#)

Version of Record: A version of this preprint was published at Nature Communications on July 4th, 2022. See the published version at <https://doi.org/10.1038/s41467-022-31594-9>.

Abstract

Brain dysfunction in myotonic dystrophy type 1 (DM1), the prototype of toxic RNA disorders, has been mainly attributed to neuronal RNA misprocessing, while little attention has been given to non-neuronal brain cells. Using a transgenic mouse model of DM1 that expresses mutant RNA in various brain cell types, we demonstrate that astrocytes exhibit impaired ramification and polarization in vivo and defects in adhesion, spreading and migration. RNA-dependent toxicity and phenotypes was also found in human transfected glial cells. In line with the cell phenotypes, molecular analyses revealed extensive expression and accumulation of toxic RNA in astrocytes, which resulted in RNA spliceopathy that was remarkably more severe than in neurons. Astrocyte missplicing affected primarily transcripts that regulate cell adhesion, cytoskeleton and morphogenesis, and it was confirmed in human brain tissue. We demonstrate for the first time that DM1 impacts astrocyte cell biology, possibly compromising their support and regulation of synaptic function.

Introduction

Brain dysfunction in neurological disease is frequently mediated by the impairment of neuronal and non-neuronal cells^{1,2}. However, the contribution of non-neuronal cells to many of these disorders has been poorly investigated. Myotonic dystrophy type 1 (DM1) is a complex multisystemic disease that affects patients of all ages^{3,4}. In addition to the typical involvement of the skeletal and cardiac muscle, the neurological manifestations are a prominent feature⁵. The DM1 cognitive profile is characterized by deficits in multiple domains, such as global cognition, intelligence, social cognition, memory, language, executive and visuospatial functioning. Personality and emotional traits include avoidant behavior, apathy anxiety-related disorders, and excessive daytime sleepiness⁶. The broad and heterogeneous cognitive neuropsychological profile of DM1 anticipates the involvement of different brain areas and neuronal circuits, a hypothesis that is corroborated by imaging studies^{7,8}

DM1 is caused by the expansion of a CTG trinucleotide in the 3' untranslated region (UTR) of the *DMPK* gene. While unaffected individuals carry 5-37 CTG repeats, pathogenic expansions are longer than 50 CTG repeats, reaching >1,000 CTG in the congenital form of the condition: larger repeats are associated with more severe symptoms and earlier onset⁹. RNAs containing expanded CUG triplets accumulate in the nucleus of DM1 cells, forming RNA foci that perturb the localization and function of RNA-binding proteins¹⁰. Among the mediators of disease, MBNL proteins are sequestered by toxic RNA foci, while CELF (CUG-BP and ETR-3-like factors) family members are upregulated. The dysregulation of these RNA-binding proteins perturbs several gene expression steps, such as transcription, alternative splicing and polyadenylation, translation, mRNA stability and mRNA intracellular localization¹¹.

In the central nervous system (CNS), *DMPK* is expressed in neuronal and non-neuronal cell types, which results in the accumulation of RNA foci in cortical neurons, astrocytes and oligodendrocytes in DM1 brains^{12,13}. However, we do not know the vulnerability of different cell types to disease, nor do we know

their role in brain dysfunction. Interestingly, *DMPK* gene expression is higher in cortical astrocytes than in neurons isolated from adult human and mouse brains^{14,15}. Mouse primary cell cultures confirmed the higher levels of *DMPK* transcripts and protein in cortical astrocytes, relative to hippocampal neurons¹⁶. Together, these results predict mechanisms of RNA toxicity in astrocytes and anticipate the involvement of this cell type in brain disease pathogenesis.

To investigate astrocyte contribution to DM1 brain disease, we used the DMSXL mouse model. Transgenic DMSXL mice carry more than 1,000 CTG repeats in the human *DMPK* locus¹⁷, display toxic RNA foci and missplicing, in association with multiple phenotypes, such as myotonia, muscle weakness, cardiac and respiratory abnormalities (Huguet et al., 2012; Panaite et al., 2013; Algalarrondo et al., 2014), as well as behavioral and electrophysiological defects in the CNS (Hernandez-Hernandez et al., 2013; Sicot et al., 2017). Foci distribution in DMSXL brains revealed higher frequency in cortical astrocytes than in neurons¹³, while co-culturing systems showed the reduced capacity of DMSXL astrocytes to protect neurons against glutamate neurotoxicity, as a result of the defective glutamate uptake²². Nevertheless, compelling evidence of astrocyte dysfunction and contribution to DM1 was lacking. In this study, we first report defective astrocyte morphology and orientation in DMSXL brains, as well as reduced astrocyte adhesion and spreading in mouse and human cell culture model systems. Mechanistically, we found robust splicing defects in astrocytes, affecting relevant transcripts that regulate cell adhesion, spreading and membrane dynamics, in line with the cellular phenotypes of these cells.

Results

Astrocytes display abnormal morphology and polarity in the brain of DMSXL mice

Given the higher frequency of nuclear RNA foci in cortical astrocytes relative to neighboring neurons that we previously observed in DMSXL mouse brains¹³, we sought to investigate the impact of the CTG repeat expansion on astrocyte phenotypes *in vivo*. We first estimated astrocyte cell density in the brain through the quantification of astrocyte markers, such as GFAP (glial fibrillary acidic protein), ALDH1L1 (aldehyde dehydrogenase 1 family member L1, a metabolic enzyme) and S100B (S100 calcium-binding protein B). Western blot revealed a significant decrease of GFAP protein levels in DMSXL frontal cortex and hippocampus, at 1 month of age (**Fig. 1a, b**). However, other canonical astrocyte markers did not show parallel downregulation, pointing to unchanged astrocyte cell density: in contrast to GFAP, ALDH1L1 was significantly upregulated in DMSXL frontal cortex and unaltered in hippocampus, while S100B levels remained unchanged in both brain regions.

To investigate the whole-cell morphology of astrocytes, we expressed cytoplasmic GFP under the control of the *Gfap* promoter using AAVs²³, in the mouse frontal cortex to observe the thin and complex ramified morphology of cortical astrocytes (**Fig. 1c**). Morphological Sholl analysis of GFP-positive astrocyte processes revealed that DMSXL astrocytes were significantly less ramified than WT astrocytes, with a more severe phenotype in processes distanced 25 μm from the nucleus. The parallel between the

shrinkage of GFP-expressing processes (**Fig. 1c**) and GFAP downregulation (**Fig. 1a, b**) indicates hypotrophy of astrocyte cytoskeleton in DMSXL brains.

Starting at the third week of postnatal development, i.e. at the time of hippocampal synaptogenesis, CA1 astrocytes of the *stratum radiatum* change the orientation of GFAP-rich stem processes to a fusiform orientation, perpendicular to the pyramidal cell layer²⁴, in a process that depends on the dynamic changes of the cytoskeleton and cell morphology. We tested whether astrocyte polarity in DMSXL hippocampus was perturbed by the expression of toxic CUG RNA, by performing GFAP immunohistochemistry in the hippocampus of DMSXL mice at 1 month (**Fig. 1d**). The extent of *stratum radiatum* astrocyte orientation was estimated by the measurement of a polarity index, corresponding to the ratio of crossing points between GFAP-positive processes and parallel or perpendicular axes to the pyramidal layer, as previously described²³. Hippocampal astrocytes of DMSXL mice showed a significant reduction in their preferential orientation regarding the pyramidal layer, when compared to WT animals, indicative of defective polarization.

In conclusion, the analysis of DMSXL brains revealed reduced astrocyte arborization and defective polarity *in vivo*, in association with lower GFAP protein levels, but no obvious signs of reduced astrocyte density.

DMSXL astrocytes show abnormal growth dynamics, reduced cell adhesion and defective cell spreading

Following the characterization of astrocyte phenotypes *in vivo*, we sought to use homogenous primary cell cultures (**Supplementary Fig. 1**), to determine to what extent CUG RNA expression affects other aspects of astrocyte cell biology and investigate the underlying mechanisms. We first assessed the global impact of the DM1 repeat expansion using xCELLigence Real-Time Cell Analysis technology, which measures the electrical impedance of cell cultures, and provides real-time, non-invasive, quantitative readouts of cell culture growth²⁵. DMSXL astrocytes exhibited a significantly lower cell index relative to control WT astrocytes (**Fig. 2a**). In contrast, impedance readings did not reveal significant changes in the population growth dynamics of primary DMSXL neurons, which remained unaltered over 72 hours in culture.

The lower cell index of DMSXL astrocytes relative to WT controls can be accounted for by multiple factors: altered proliferation and cell cycle dynamics, increased cell death, abnormal adhesion and/or spreading of cultured cells. We investigated the contribution of each one of these factors to the abnormal growth of DMSXL astrocyte cultures. To analyze cell proliferation, we synchronized primary astrocytes by serum deprivation prior to bromodeoxyuridine (BrdU) incorporation and detection assay, combined with propidium iodide (PI) counterstaining to evaluate DNA content. Fluorescence-activated cell sorting (FACS) did not reveal significant changes in the distribution between different phases of the cell cycle, hence excluding abnormal cell cycle progression of primary DMSXL astrocyte cultures (**Fig. 2b**). We next tested the contribution of cell death by AnnexinV binding and PI incorporation, indicators of early apoptotic and

late cell death, respectively. Similarly, FACS showed no difference in the number of AnnexinV- and PI-positive cells between DMSXL and WT astrocytes under basal culture conditions (**Fig. 2c**). To test if DMSXL astrocytes were more vulnerable to stress, we treated cultures with staurosporine to induce apoptosis. Staurosporine enhanced the levels of cell death in both genotypes to a similar extent (**Fig. 2c**). In conclusion, primary DMSXL astrocyte cultures displayed reduced growth, illustrated by abnormal impedance readings, which did not result from abnormal cell cycle progression or increased cell death.

We next asked if the lower cell index of DMSXL astrocytes could be a consequence of modified cell-substrate interactions. We plated primary DMSXL or WT astrocytes and monitored their adhesion and spreading by live cell videomicroscopy²⁶. To exclude the confounding effect of different starting cell numbers, we first confirmed that the cell density of DMSXL and WT cultures was identical 45 minutes after plating (**Fig. 3a**). In spite of the same number of cells initially plated and attached to the substrate, the total surface occupied by DMSXL astrocytes was lower 45 minutes after plating relative to control WT cultures (**Fig. 3b**). The lower confluence of DMSXL astrocytes persisted up to 48 hours (**Fig. 3c**). In contrast, DM20 astrocyte cultures, derived from mice overexpressing short *DMPK* transcripts with 20 CTG repeats²⁷, exhibited normal growth profiles over time (**Fig. 3d**), indicating that the reduced confluence of DMSXL astrocytes could not be accounted for by *DMPK* overexpression alone. Finally, we confirmed the defective spreading and abnormal morphogenesis of DMSXL astrocytes, by measuring cell size over time and the growth rate of individual living cells, by semi-automated videomicroscopy (**Fig. 3e**). We found significantly reduced cell sizes, as well as a lower rate of cytoplasm spreading of primary DMSXL astrocytes, relative to WT controls (**Fig. 3f**). Pairwise comparisons revealed that the surface of DMSXL astrocytes was ~30-40% smaller throughout the 12-hour period.

We validated the impact of toxic RNA on the cell adhesion and spreading of a human glial cell model of DM1. We used stably transfected MIO-M1 cells, which expressed a large CTG repeat expansion and accumulated abundant nuclear RNA foci, following the induction of a doxycycline-responsive promoter (**Supplementary Fig 2a**). We induced transgene expression for 24 hours prior to replating and monitoring of cell adhesion, spreading and morphology by live cell videomicroscopy (**Supplementary Fig 2b**). Doxycycline-treated MIO-M1 cells expressing toxic CUG transcripts showed decreased cell spreading relative to non-induced cells over a period of 12 hours (**Supplementary Fig 2c**). Pairwise comparisons revealed that the average cell sizes were reduced by ~35% in CUG-expressing cells at 9 and 12 hours after plating.

In summary, DM1 repeat expansion affects the adhesion, spreading and morphogenesis of mouse and human glial cells in culture.

Defective adhesion and spreading of DMSXL astrocytes are associated with abnormalities in focal adhesion organization, cytoskeleton reorientation and cell migration

Cell-substrate adhesion relies on focal aggregates of specialized proteins that serve as structural links between the cytoskeleton and the extracellular matrix. To gain insight into the subcellular structures contributing to the adhesion and spreading phenotypes of DMSXL astrocytes, we quantified focal adhesions in cultured cells. We stained clusters of vinculin, one of the first proteins to be recruited to assembling focal adhesion complexes and that has an important role in maintaining focal contacts²⁸. We used phalloidin to stain the actin cytoskeleton (**Fig. 4a**). The quantification of vinculin clusters revealed a significantly lower number of focal adhesions per cell in DMSXL astrocytes, relative to WT controls (**Fig. 4b**), in spite of similar expression levels of total vinculin (**Fig. 4c**), suggesting disrupted assembly and maintenance of focal adhesion structures. Using the actin fluorescent signal, we measured cell surface and confirmed the reduced size of individual DMSXL astrocytes 3 h after plating (**Fig. 4d**).

Focal adhesions play an integral role in cell polarity and migration. Therefore, we asked if the reduced density of focal adhesions in DMSXL astrocytes affected their polarity and migration. One of the most frequently used culture systems to explore cell polarity and migration in culture is the scratch injury assay, during which cells reorient and extend towards the wound²⁹. Prior to migration, the cell reorganizes the microtubule-organizing center (MTOC) and Golgi apparatus in front of the nucleus to face the free space, hence directing the membrane protrusion at the leading-edge perpendicular to the wound. We performed a wound healing assay to assess DMSXL astrocyte polarization and migration in culture. Following the scratch, we monitored DMSXL astrocyte reorientation by immunofluorescence staining of the Golgi apparatus and centrosome and found a mild but significant defect in astrocyte polarization (**Fig. 4e**): overall while $62.8\% \pm 1.6\%$ of WT astrocytes orientated their Golgi apparatus and centrosome perpendicularly to the wound, only $55.7\% \pm 0.8\%$ of DMSXL astrocytes were correctly orientated. Next, we examined the impact of defective assembly of focal adhesions and cell reorientation on cell migration, by time-lapse videomicroscopy and tracking of the trajectories of individual astrocytes (**Fig. 4f**): DMSXL astrocytes migrated at a higher speed over 50 hours of wound closure (**Fig. 4g**) and displayed more random movement characterized by a higher mean square displacement (**Fig. 4h**), indicating that they covered a larger surface area over time until they filled the wound completely, when compared to WT control astrocytes.

The labeling of cell-substrate adhesions and the monitoring of cell movement revealed that the DM1 expansion mutation affects focal adhesion assembly, the re-orientation of the cytoskeleton and the directionality of cell migration in DMSXL astrocytes.

DMSXL astrocytes show high expression of toxic RNA and abundant nuclear foci

We used homogenous primary cultures to assess the toxicity of CUG RNA repeats and investigate the molecular bases underlying the pronounced phenotypes of DMSXL astrocytes. We quantified the expression of expanded *DMPK* transcripts in primary cultures derived from homozygous DMSXL mice, following 6, 12 and 30 days *in vitro* (*DIV*). Transgene expression was significantly higher in DMSXL

astrocytes: *DMPK* expression levels were four- to 12-fold higher in astrocytes than in neurons (**Fig. 5a**, top panel). As expected, *DMPK* transgene expression profiles followed the endogenous *Dmpk* gene in both types of brain cells; murine *Dmpk* gene expression was also significantly higher in astrocytes, relative to neurons (**Fig. 5a**, bottom panel). In agreement with higher transgene expression, FISH confirmed a higher percentage of DMSXL astrocytes showing RNA foci, and a higher number of foci per cell, when compared to DMSXL neurons (**Fig. 5b**).

We investigated if CUG foci accumulation in primary DMSXL brain cells affected the canonical splicing regulators associated with DM1 RNA toxicity. Fluorescent immunodetection revealed marked cytoplasmic localization of MBNL1 and MBNL2 in primary brain cells (**Fig. 5c**). While both MBNL1 and MBNL2 co-localized with RNA foci in DMSXL astrocytes, only MBNL2 displayed clear co-localization with RNA foci in neurons. Western blot revealed no obvious changes in CELF1 and CELF2 protein levels in DMSXL astrocytes and DMSXL neurons (**Fig. 5d**), relative to WT control cells.

Together with their pronounced phenotypes, primary DMSXL astrocytes expressed higher levels of expanded and toxic CUG-containing *DMPK* transcripts, exhibited more pronounced accumulation of toxic RNA foci with MBNL protein sequestration, when compared to primary DMSXL neurons, which did not display overt population growth phenotypes.

DMSXL astrocytes exhibit significant splicing variations of genes involved in cell adhesion, cytoskeleton and cell membrane dynamics

To decipher the mechanisms behind abnormal adhesion and spreading of DMSXL astrocytes, we performed RNA sequencing of primary cells. Transcripts from a total of 16,878 genes were detected in primary mouse astrocytes. The most severe changes in expression were revealed by a fold change threshold of at least 1.4 and a *p* value (corrected for multiple comparisons) < 0.05. Under these stringent selection criteria, only five transcripts showed significant expression changes in primary DMSXL astrocytes (**Supplementary Table 1**). Similarly, using a selective threshold of 10% change in PSI (percentage of splicing inclusion) and *p* value (corrected for multiple comparisons < 0.05, we found evidence of missplicing in 128 astrocyte transcripts, including abnormalities in exon skipping, splicing of mutually exclusive exons, splicing of multiple exons, as well as changes in the selection of acceptor and donor sites (**Supplementary Table 2**). The same thresholds revealed expression abnormalities in two genes, and splicing defects in 12 transcripts among the 17,089 transcripts identified in primary DMSXL neurons (**Supplementary Table 3, 4**).

To investigate the biological functions associated with the 128 transcripts misspliced in primary DMSXL astrocytes, we performed gene ontology (GO) enrichment analyses and found 69 biological processes, 68 cellular components and 9 molecular functions significantly overrepresented. Post-processing methods identified cell adhesion, cytoskeleton and plasma membrane as the low redundancy terms most frequently associated with enriched biological processes, cellular components and molecular functions in

primary DMSXL astrocytes (**Fig. 6a**). We then selected transcripts associated with representative GO terms for validation of abnormal exon skipping (**Supplementary Table 5**) and confirmed the significant missplicing of all the exons tested in primary DMSXL astrocytes (**Fig. 6b**). In contrast, the majority of these transcripts remained unaffected in primary DMSXL neurons: among the genes studied, modest splicing dysregulation was only detected in *Capzb* and *Itga6* transcripts by RT-PCR (**Supplementary Fig. 3a**).

We confirmed the spliceopathy of relevant transcripts associated with cell adhesion and cytoskeleton *in vivo*, through the analysis of DMSXL frontal cortex (**Fig. 6c, Supplementary Fig. 3b**) and hippocampus (**Fig. 6d, Supplementary Fig. 3c**). However, the extent of the splicing defects in whole tissues was modest, as demonstrated by the lower changes in PSI between genotypes. Among all the eleven alternative exons studied, four were significantly dysregulated in DMSXL frontal cortex, while seven were abnormally spliced in DMSXL hippocampus.

The heterogeneity and intermixing of diverse cell types in complex tissues, such as the brain, may dilute severe missplicing events confined to specific cell populations, and it complicates the attribution of the splicing abnormalities to individual cell types. We specifically investigated splicing dysregulation in cortical astrocytes *in vivo*, isolated from 1-month-old DMSXL mice with antibody-coupled magnetic beads. The enrichment of the astrocyte cell fraction was confirmed by the semi-quantitative expression analysis of *Gfap* transcripts mainly expressed in astrocytes, while the non-astrocyte fraction showed high expression of neuron-specific *Syp* (synaptophysin) and oligodendrocyte-specific *Gpr17* (G-coupled protein receptor 17) RNA (**Supplementary Fig. 3d**). We then compared the splicing of adhesion- and cytoskeleton-associated transcripts between the astrocyte-enriched fraction and the non-astrocyte flow-through (consisting of neurons, oligodendroglia and endothelial cells). The severe spliceopathy in DMSXL cortical astrocytes *in vivo* was demonstrated by the significant missplicing of nine out of eleven alternative exons studied, while only two were significantly misspliced in non-astrocyte cells (**Fig. 6e**). In other words, the splicing analysis in cortical astrocytes isolated from DMSXL brains revealed pronounced splicing defects that were undetected in whole brain tissue samples, indicating localized RNA toxicity in astroglia.

In summary, we found compelling evidence of pronounced splicing dysregulation in DMSXL astrocytes of genes involved in cell adhesion, cytoskeleton organization and membrane dynamics, in agreement with the cellular phenotypes.

Human DM1 brains show pronounced foci accumulation in astrocytes and splicing dysregulation of adhesion and cytoskeleton-related transcripts

To determine if the insight gained from DMSXL astrocytes is relevant for human disease we examined post-mortem human frontal cortex. We first investigated if the higher abundance of nuclear RNA foci in cortical astrocytes relative to neighboring neurons observed in DMSXL mouse brains¹³ was also detected in human disease brains. FISH detection of expanded *DMPK* transcripts in human DM1 frontal

cortex confirmed a higher frequency of foci and a higher number of foci per nucleus in GFAP-expressing astrocytes, relative to MAP2-stained neurons (**Fig. 7a, b; Supplementary Fig. 4a**). In spite of inter-individual variability, the expression of astrocyte protein markers in human brains followed the variation trends found in DMSXL mice: a tendency for lower GFAP expression and higher ALDH1L1 levels (**Fig. 7c; Supplementary Fig. 4b**). We finally investigated if the target exons identified in DMSXL astrocytes were similarly dysregulated in DM1 brains. Overall, seven out of the ten target exons studied, were significantly misspliced in adult DM1 brain, compared to non-DM controls (**Fig. 7d**). Two other splicing events (*ITGB4* exon 35 and *MPDZ* exon 28) also showed a clear trend, but did not reach statistical significance.

The brains of DM1 patients exhibited marked RNA foci accumulation in astrocytes and confirmed the missplicing of transcripts relevant for cytoskeleton, cell adhesion and morphology.

Discussion

The initial research on DM1 brain disease was grounded on the idea that repeat-induced missplicing in neurons was the dominant event at the origin of neuropsychiatric symptoms^{12,30}. Previous attempts to unveil glial involvement in human DM1 brains yielded inconclusive results⁷. Using a mouse model of DM1, we previously reported Bergmann glia abnormalities in the cerebellum, which affected the activity of Purkinje cells²². Here, we uncovered the general vulnerability of astrocytes to CUG RNA toxicity. We showed that the DM1 repeat expansion impacts critical structural and functional features of astrocytes, such as cell morphology, adhesion and orientation.

Pronounced RNA toxicity in astrocytes is accompanied by defects in cell adhesion and spreading. Primary DMSXL astrocytes express higher levels of *DMPK* transgene and exhibit greater foci abundance than DMSXL neurons, likely contributing to the more severe spliceopathy and overt phenotypes of astroglia. In agreement with defective cell spreading and reduced size growth of primary DMSXL astrocytes, RNA sequencing uncovered a significant number of misspliced transcripts associated with cell adhesion, cytoskeleton and cell membrane, which we confirmed to be enriched in cortical DMSXL astrocytes, relative to the remaining brain cells.

The abnormal splicing of *Itga6* and *Itgb4* in DMSXL astrocytes may perturb focal adhesion assembly and subsequent cell spreading. Indeed, exon 27 of *ITGA6* is regulated by MBNL1³¹, and it encodes a cytoplasmic protein domain involved in the transmission of biochemical and mechanical signals from the extracellular matrix to the cytoskeleton³². A role of MBNL proteins in the regulation of integrin-mediated adhesion was previously described in *Drosophila*³³ and in human cells³⁴. In addition, MBNL1 targets have also proposed roles in cytoskeletal rearrangements and post-mitotic cell growth^{31,35}. We suggest that MBNL protein inactivation by RNA foci in DMSXL astrocytes is a determinant event behind reduced cell adhesion, spreading and growth, and that the coordinated dysregulation of gene sets associated with adhesion and integrin binding represents an integral feature of disease pathogenesis in multiple cell types and tissues.

Integrins and other cell adhesion molecules at neuroglial contacts are instrumental for the synaptic coverage by the astrocyte fine processes, and the control of synaptic transmission and plasticity. Defects in integrin expression and localization have been linked to abnormal social and stress behavior, reduced spatial and working memory and to autism spectrum disorder³⁶, neuropsychological features that have been reported in DM1 patients to different extents⁶. Importantly, abnormal focal adhesion signaling in the CNS causes neuronal hyperexcitability and seizure activity in *Drosophila*³⁷, and it may contribute to the increased sensitivity to induced seizures of DMSXL mice³⁸.

The cytoskeleton plays an instrumental role in the establishment of intrinsic cell polarity. The perturbation of microtubule dynamics, through changes in the activity of microtubule-binding proteins, impairs proper cell polarization³⁹. The missplicing of a significant number of transcripts coding for tubulin-binding proteins and regulators of microtubule dynamics in DMSXL astrocytes may therefore contribute to the misorientation of the microtubule-organizing center (MTOC) and the erratic migration during the wound healing assay. Changes in the activity of CLASP1, for example, were shown to cause random cell movement in culture, similar to those detected in DMSXL astrocytes⁴⁰; SORBS1 regulates cell adhesion, spreading and migration⁴¹; and NUMA1 controls cell polarity and the dynamics of microtubules⁴². The uncontrolled cell movement and increase speed of DMSXL astrocytes, may also result from the low number of stable focal adhesions, which under normal conditions tend to inhibit cell migration⁴³. Defects in brain cell migration have been associated with multiple neurological disorders, characterized by abnormal cortical function, cognitive and motor impairment, as well as epilepsy⁴⁴.

The complex morphology of astrocytes is a defining feature of their function and it is controlled by extensive cytoskeleton remodeling. Mature astrocytes grow numerous thin processes that reach out to occupy individual, non-overlapping spatial domains in the brain. Through their sophisticated ramification, astrocytes provide extensive coverage of neighboring synapses to guarantee efficient neurotransmitter clearance, ion homeostasis, metabolic support and gliotransmitter availability to neurons⁴⁵. At birth, astrocyte processes contain primarily microtubules, which are later replaced by GFAP-containing intermediate filaments⁴⁶. The missplicing of microtubule-associated genes, together with the lower levels of GFAP may contribute to the reduced arborization of cortical astrocytes in DMSXL brains. Since GFAP is constitutively expressed in the main processes of white matter astrocytes⁴⁷, GFAP downregulation is indicative of localized astrocyte hypotrophy in white matter.

As the most abundant glial cell type in the mammalian brain, astrocytes are integral to the regulation of brain wiring and function. In light of their role in the formation, maintenance and control of synapses, it is not surprising that their dysfunction is an important contributor to many neurological diseases, including Alzheimer, Parkinson and Huntington disease, amyotrophic lateral sclerosis, spinal muscular atrophy, epilepsy, and fragile X syndrome⁴⁸. In most conditions, astrocyte dysfunction is accompanied by changes in the expression of ion channels, neurotransmitter transporters, membrane receptors or intracellular proteins⁴⁹.

Alternatively, since astrocyte-neuron communication is intimately dependent on the specialized morphology of both cell types, aberrant astrocyte ramifications are predicted to be detrimental for brain neurophysiology. Appropriate astrocyte reorientation is critical for synaptic maturation²⁴. In particular, post-natal structural rearrangements increase the proximity between parallel astrocyte processes and synaptic terminals, to enhance synaptic coverage and facilitate ion buffering, the release of neurotrophic factors and the uptake of neurotransmitters by astrocytes⁵⁰. In this context, the impaired astrocyte arborization and polarity in DMSXL hippocampus may not only reduce the direct contacts between astrocyte processes and neuronal dendrites, but also impact the efficiency of synaptic transmission, contributing to the altered neuronal plasticity of DMSXL mice¹³.

Neuroimaging studies have suggested early white matter involvement in DM1, whereas age-dependent cortical gray matter loss may occur later in the disease process in association with neurodegeneration⁷. Early astrocyte atrophy with decreased GFAP staining has been described in some mouse models of Alzheimer Disease⁵¹ and in the prefrontal cortex of young patients suffering from major depressive disorder⁴⁹. It has been proposed that astrocyte atrophy in frontal cortex impacts the capacity of astroglia to maintain brain homeostasis, contributing to the expression of depression-like phenotypes, such as anhedonia⁵², a behavioral feature of DMSXL mice¹³ and DM1 patients⁵³.

In conclusion, our results demonstrate the pronounced impact of DM1 toxic RNA on astrocyte cell biology. Altered adhesion of astrocytes in DM1 could affect their migration, orientation and integration into the complex microenvironment of the brain, hence impairing neural wiring and synaptogenesis. Future therapeutic strategies targeting the CNS must consider the restoring of astrocyte-mediated homeostasis, in conjunction with neuronal rescue and repair strategies.

Methods

Transgenic mice

DMSXL and DM20 transgenic mice (>90% C57BL/6 background) carry 45 kb of human genomic DNA from a DM1 patient or a healthy control individual, respectively^{17,27}. The DMSXL mice used in this study carry more than 1500 CTG repeats within the *DMPK* transgene, while DM20 mice carry a short 20 CTG repeat sequence. Transgenic DM20 status was assessed as previously reported¹³. DMSXL status was assessed by multiplex PCR using the oligonucleotide primers, which hybridize the *DMPK* transgene and the transgene integration site in the mouse *Fbxl7* gene: FBF (forward, TCCTCAGAAGCACTCA TCCG), FBFBR (reverse, AACCTGTATTTGACCCAG) and FBWDR (reverse, ACCTCCATCCTTTTCAGCACC). FBF and FBFBR primers hybridize the mouse *Fbxl7* gene, amplifying a sequence of 167 bp in WT mice. FBWDR primer hybridizes specifically the human transgene, generating a 236 bp PCR product.

This project was conducted according to the ARRIVE guidelines (Animal Research: Reporting *In Vivo* Experiments), with the authorization for animal experimentation n° 75 003 in the animal facility with

the approval n°: B 91 228 107 both delivered by Prefecture de police and the French veterinary department.

Human tissue samples

Human frontal cortex samples were collected from different laboratories: Dr. Yasuhiro Suzuki (Asahikawa Medical Center, Japan) and Dr. Tohru Matsuura (Okayama University, Japan). All experiments using human samples were approved by the Ethics Committees of the host institutions. Written informed consent of specimen use for research was obtained from all patients. Information relative to patients was previously described^{13,22}.

Primary astrocytes cell culture

Primary dissociated cell cultures of cortical astrocytes were prepared from postnatal day 1 WT and DMSXL mouse littermates. After carefully removing the meninges in Leibovitz L- 15 Medium (Life Technologies; 11415049) supplemented with 30 μ M Glucose (Sigma-Aldrich; 49139), the cortices were mechanically dissociated and cultured for 2 weeks in DMEM low glucose (Life Technologies, 31885-023), supplemented with 10% FBS and 0.05 mg/ml gentamycin (Life Technologies; 15710). All experiments were performed using 2 weeks-cultured primary astrocytes, unless stated otherwise.

Primary neurons cell culture

Primary dissociated cell cultures of cortical neurons were prepared from embryonic day 16.5 WT and DMSXL littermates. After carefully removing the meninges in Glucose-supplemented Leibovitz L-15 medium, the cortices were washed twice with Neuronal medium: Neurobasal- A (Life Technologies; 10888022), supplemented with 1X B27 supplement (Life Technologies; 17504044), 0.5 mM L-Glutamine (Life Technologies; 25030024), 1% antibiotic and antimycotic (Life Technologies; 15240-096). Cortices were then incubated 15 min in Neuronal medium containing Trypsin (Life Technologies; 25300096) and DNaseI (Sigma-Aldrich; 11284932001) and washed with Neuronal medium supplemented with 5% FBS. After mechanical dissociation, cells were washed twice and counted before plating in suitable dishes coated with Poly-D-lysine (Sigma-Aldrich; P6407) and Laminin (Sigma- Aldrich; L2020) in Neuronal medium containing 5% FBS. Medium was changed 4 h after plating to Neuronal medium supplemented with 5 μ M AraC (Sigma-Aldrich; C6645-25MG) and without FBS to avoid astrocytes proliferation. Half of the medium was changed each 3-4 days.

Fluorescent in situ hybridization (FISH) and Immunofluorescence

Primary cells were fixed at 2 weeks *in vitro* for 15 min in 4% PFA (VWR; J61899.AP) and ribonuclear inclusions were detected using a 5'-Cy3-labelled (CAG)₅ PNA probe, as previously described¹⁸. Immunofluorescence (IF) combined with fluorescent in situ hybridization (FISH) was performed as previously described¹³. Primary antibodies used are the following: Tuj1/ β - tubulinIII (Covance; PRB-435P), GFAP (Dako cytometry; Z0334), MBNL1 and MBNL2 (G. Morris; Keele University, UK), Vinculin (Sigma-Aldrich V9131), GM130 (BD laboratories; 610822) and Pericentrin (Covance; PRB432C).

Microscope imaging and image analysis

Images were acquired with a Zeiss ApoTome 2 fluorescent microscope or a Leica SP8 SMD confocal microscope (x63 and x40 objectives). RNA foci were counted in 3D stacks using the Spot Detector plugin of the ICY bioimageanalysis open source program (<http://icy.bioimageanalysis.org>). MBNL1 and MBNL2 nucleo-cytoplasmic ratio was quantified on confocal images using nuclear DAPI or MBNL signal to create a mask of the nucleus and cytoplasm respectively, and to measure the MBNL1 and MBNL2 intensity inside the mask. Focal adhesions formation was quantified as previously described⁵⁴, by measuring the number of Vinculin-rich clusters at 3 h post plating on confocal z stack projections, after background subtraction using rolling ball method, gamma adjustment of 1.4 and analysis of particles between 0.1 and 40 μm^2 . IF and FISH images were treated with Fiji - ImageJ software⁵⁵ to create the figures.

RNA isolation, cDNA synthesis and RT-PCR analysis

RNA extraction was performed with the RNeasy Mini kit (QIAGEN; 74104) following the manufacturer's protocol, including a DNase digestion step (RNase-Free DNase Set; QIAGEN; 79254) after the first wash with RW1 buffer. RNA concentration was assessed using the NanoDrop (Thermo Scientific) and RNA quality was verified by electrophoresis on an agarose gel. cDNA synthesis and semi-quantitative reverse-transcriptase PCR analysis of alternative splicing were performed as previously described^{13,22}. Oligonucleotide primers used for RT-PCR analysis are indicated in **Supplementary Table 6** (mouse samples) and **Supplementary Table 7** (human samples).

Quantitative RT-PCR.

Human *DMPK*, murine *Dmpk* and *18S* internal control transcripts were quantified in a 7300 Real Time PCR System (Applied Biosystems) with a Power SybrGreen detection method (Thermo Scientific; 4367659) using oligonucleotide primers and conditions previously described¹⁸.

Western blots

Proteins from primary cells and mouse and human brain tissues were extracted using RIPA buffer (Thermo Scientific; 89901) supplemented with 0,05% CHAPS (Sigma; C3023), 1x complete protease inhibitor (Sigma-Aldrich; 04693124001) and 1x PhosSTOP phosphatase inhibitor (Sigma; 04906845001). Protein concentrations were determined using the Pierce BCA Protein Assay Kit (Thermo Scientific; 23227). Between 10 and 40 µg proteins were mixed with 2X Laemmli Sample Buffer (Sigma; S3401), denatured for 5 min at 95 °C and resolved in 10% TGX Stain-Free polyacrylamide gels (Bio-Rad; 1610183). After electrophoresis, gels were activated for 2 minutes under UV light, proteins were transferred onto Nitrocellulose membranes using Trans-Blot® Transfer System (Bio-Rad) and total protein on the membrane was imaged using the ChemiDoc Imaging System (Bio-Rad). Membranes were then blocked in 2.5-5% Blotto non-fat dry milk (Santa Cruz Biotech; sc2325) in 1x TBS-T (10 mM Tris-HCl, 0.15 M NaCl, 0.05% Tween 20) during 1 h at room temperature (RT) and incubated with the primary antibody over night at 4 °C. After three washes in TBS-T membranes were incubated with IRDye® 800CW donkey anti-rabbit (LI-COR Biosciences; P/N 926-32213) or 680RD donkey anti-mouse (LI-COR Biosciences; P/N 926-68072) for 1 h at RT, washed three times and imaged using LI-COR Odyssey® CLx Imaging System. Band intensity was quantified using Image Studio Lite. Primary antibodies are indicated in **Supplementary Table 8**. Normalized protein expression levels are expressed relative to the average of control samples.

Impedance-based real-time monitoring of cell adhesion and growth

Cell population adhesion and growth was monitored using the *xCELLigence* RTCA MP system (ACEA Biosciences Inc), which measures the electrical impedance of the cells in real time, translated into a cell index proportional to the number, surface or adhesion strength of the plated cells. Primary neurons (200.000 cells/well) were plated onto Poly-D-lysine and Laminin coated E-plates (Ozyme; 5232368001) while primary astrocytes (20,000 cells/well) were plated on uncoated E-plates. After a 30-minute settling of the cells at RT, impedance was measured each 5 minutes during the first 8 h and each 15 min for the following 72 h, inside the incubator.

FACS analysis of astrocytes cell cycle

Primary astrocytes were arrested in G0 by completely removing the serum from the culture medium for 24 h. After cell cycle release in medium containing 5% of FBS, cells were incubated with 10 µM Bromodeoxyuridine (BrdU) (Euromedex; NU-122S) for 1 h, trypsinized, fixed O/N in 70% ethanol at -20 °C, and stained with antiBrdU-FITC (BD Horizon; 347583) and 3 µM propidium iodide (PI) (Sigma; P4170), before FACS detection of BrdU-FITC and PI in 10,000 cells per embryo. Three different biological

replicates were analyzed per genotype. Cell cycle phases were considered as follows: G1-phase cells are BrdU negative with low PI staining (200 intensity units), S-phase cells are BrdU positive and show a range of low to high PI intensity (200 to 400 intensity units) and G2/M cells are BrdU negative with high PI intensity (400 intensity units).

FACS analysis of astrocytes death

Cell death was analyzed in astrocytes at 3 days post plating after O/N incubation with DMSO (solvent control) or 0.5 μ M Staurosporine (Euromedex; LS9300-A). Cells were trypsinized, counted and 10⁶ cells were stained with a mix of 5% Annexin V-FITC (BD Horizon; 556547) to detect apoptotic cells, PI to detect necrotic cells and 2.5 % Cd11b-V450 (BD Horizon; 560456) to exclude possible microglia contamination. Staining was performed for 15 min, prior to FACS analysis of 10,000 cells per embryo. Six different biological replicates were analyzed per genotype. The percentage of AnnexinV-positive, PI-positive WT and DMSXL astrocytes (negative for Cd11b staining) was analyzed in DMSO and Staurosporine conditions.

Videomicroscopy monitoring of cells dynamics

Primary astrocyte adhesion and spreading was monitored using the IncuCyte Zoom video-microscope (Essen BioScience) after seeding 20,000 cells/well in 96-wells plates and taking phase-contrast pictures every 45 minutes. Cell confluence was determined using the IncuCyte ZOOM basic analysis method. Cell surface was measured by manual tracing. Cell number was counted manually using Image J. Experiments were performed in triplicate. Astrocytes migration was assessed using the Cell Migration Assay kit and migration module of the IncuCyte followed by manual tracking of the astrocytes using Fiji Manual Tracking plugin and quantitative analysis of speed and mean square displacement, using DiPer macro on Microsoft Office Excel, as previously described ⁵⁶.

RNA sequencing

RNA samples were prepared from WT and DMSXL primary astrocytes, grown for 15 days *in vitro*. Illumina-compatible precapture barcoded mRNA libraries were constructed, and a series of 24 barcoded libraries was pooled at equimolar concentrations. The capture process was performed according to the manufacturer's protocols for TruSeq Stranded mRNA (Illumina) and sequencing on an Illumina HiSeq2500. Global gene expression was analysed as previously described ⁵⁷ using the DESeq2 package. Significant expression changes were considered for further analysis if fold change between genotypes > 1.4, and *p* value (corrected for multiple comparisons) <0.05. Alternative splicing analyses were performed using the open source FARLINE pipeline (http://kissplice.prabi.fr/pipeline_ks_farline) as previously

described^{58,59}. Significant missplicing events were selected for further analysis if the percentage of splicing inclusion between genotypes > 10 and p value (corrected for multiple comparisons) < 0.05 (general linear mode). Percentage of splicing inclusion (PSI) was calculated as (inclusion of alternative exon)/[(inclusion of alternative exon)+(exclusion of alternative exon)].

Gene ontology analysis

Gene ontology (GO) analyses were performed using Webgestalt tool⁶⁰ to identify significant functional enrichment in three GO categories: biological processes, cellular component and molecular function. FDR < 0.01 and gene number ≥ 2 were defined as selection criteria for further analyses. Post-processing weight set cover methods were used to summarize and reduce the redundancy, through the identification of the most representative GO terms.

Acute isolation of cortical astrocytes from mouse brain

Brains from 1-month-old mice were dissected and the cortices were enzymatically and mechanically dissociated using the adult brain dissociation kit (Miltenyi; 130-107-677), following the manufacturer's protocol. The astrocytes were isolated from the resulting single cell suspension using magnetic anti-ACSA-2 labelled microbeads (Miltenyi; 130-097-678) for positive selection, following the manufacturer's protocol. The cells in the ACSA-2 positive cell fraction (retained in the column) and ACSA-2 negative cell fraction (flow through) were counted and a cell pellet was collected by centrifugation at 300 g for 5 min. The supernatant was removed, and the cell pellets were frozen at -80 °C until further use. The sequences of the oligonucleotide primers used in the RT-PCR analysis of astrocyte enrichment are listed in **Supplementary Table 9**.

Analysis of astrocyte morphology in vivo

Complex astrocyte morphology *in vivo* was studied as previously described⁶¹. Briefly, four-week-old mice were deeply anaesthetized by a mixture of ketamine and xylazine and placed in a stereotaxic frame. AAV expressing a cytoplasmic GFP protein under the GFAP promoter was delivered into the mouse frontal cortex with a 34-gauge blunt-tipped needle linked to a 2 μ L Hamilton syringe by a polyethylene catheter at the following stereotaxic coordinates: AP: -0.9 mm; L:-1 mm to the bregma at a depth of -2.75 mm to the skull. The needle was left in place for 5 min and was slowly withdrawn. Animals were sacrificed 15 days after injection. Z-stack images were acquired at a confocal microscope with a $\times 40$ magnification (Leica SP5 inverted confocal). Isolated astrocytes were selected based on their GFP staining. The ImageJ plugin "Sholl analysis"⁶² was used to measure the number of intersections between GFP stained processes and concentric circles spaced by 5 μ m and centered on astrocyte nucleus.

Statistical analysis.

Statistical analyses were performed with Prism (GraphPad Software, Inc). Data are presented as mean \pm standard error of means (\pm SEM). Individual datapoints are shown in graphs, except if it compromises clarity. Tukey box-and-whiskers plots are used to represent large numbers of replicates ($n > 20$) to improve clarity. Chi-square test was used to compare categorical variables between two groups. After performing a normality test on the numeric variables, we used two-tailed Student's *t* test for parametric data and Mann-Whitney *U* test for non-parametric data, when two groups were compared. When three or more groups were compared, we performed a one-way ANOVA or Repeated-measures ANOVA on parametric data, or Kruskal-Wallis test on non-parametric data. We used two-way ANOVA to assess the statistical interaction between two independent variables. *Post hoc* pairwise comparisons were performed to account for multiple comparisons. *, $p < 0.05$; **, $p < 0.01$, ***, $p < 0.001$.

Data availability

The authors declare that all data supporting the findings of this study are available within the paper and its supplementary information files. All the RNA sequencing data sets that were used as input for the study are available at the following link:

<https://www.ncbi.nlm.nih.gov/geo/query/acc.cgi?&acc=GSE162093>.

References

1. Gleichman, A. J. & Carmichael, S. T. Glia in neurodegeneration: Drivers of disease or along for the ride? *Neurobiol. Dis.* **142**, 104957 (2020).
2. Chung, W. S., Welsh, C. A., Barres, B. A. & Stevens, B. Do glia drive synaptic and cognitive impairment in disease? *Nat. Neurosci.* **18**, 1539–1545 (2015).
3. Udd, B. & Krahe, R. The myotonic dystrophies: Molecular, clinical, and therapeutic challenges. *Lancet Neurol.* **11**, 891–905 (2012).
4. Harper, P. S. *Myotonic Dystrophy*. (W. B. Saunders, 2001).
5. Gourdon, G. & Meola, G. Myotonic dystrophies: State of the art of new therapeutic developments for the CNS. *Front. Cell. Neurosci.* **11**, 101 (2017).
6. Okkersen, K. *et al.* The cognitive profile of myotonic dystrophy type 1: A systematic review and meta-analysis. *Cortex* vol. 95 143–155 (2017).
7. Minnerop, M., Gliem, C. & Kornblum, C. Current progress in CNS imaging of myotonic dystrophy. *Front. Neurol.* **9**, 646 (2018).

8. Serra, L. *et al.* Abnormal functional brain connectivity and personality traits in myotonic dystrophy type 1. *JAMA Neurol.* **71**, 603–611 (2014).
9. De Antonio, M. *et al.* Unravelling the myotonic dystrophy type 1 clinical spectrum: A systematic registry-based study with implications for disease classification. *Rev. Neurol. (Paris)*. **172**, 572–580 (2016).
10. Braz, S. O., Acquaire, J., Gourdon, G. & Gomes-Pereira, M. Of Mice and Men: Advances in the understanding of neuromuscular aspects of myotonic dystrophy. *Frontiers in Neurology* vol. 9 519 (2018).
11. Sznajder, Ł. J. & Swanson, M. S. Short tandem repeat expansions and RNA-mediated pathogenesis in myotonic dystrophy. *Int. J. Mol. Sci.* **20**, 3365 (2019).
12. Jiang, H., Mankodi, A., Swanson, M. S., Moxley, R. T. & Thornton, C. A. Myotonic dystrophy type 1 is associated with nuclear foci of mutant RNA, sequestration of muscleblind proteins and deregulated alternative splicing in neurons. *Hum. Mol. Genet.* **13**, 3079–3088 (2004).
13. Hernández-Hernández, O. *et al.* Myotonic dystrophy CTG expansion affects synaptic vesicle proteins, neurotransmission and mouse behaviour. *Brain* **136**, 957–970 (2013).
14. Zhang, Y. *et al.* An RNA-sequencing transcriptome and splicing database of glia, neurons, and vascular cells of the cerebral cortex. *J. Neurosci.* **34**, 11929–11947 (2014).
15. Zhang, Y. *et al.* Purification and Characterization of Progenitor and Mature Human Astrocytes Reveals Transcriptional and Functional Differences with Mouse. *Neuron* **89**, 37–53 (2016).
16. Ophuis, R. J. A. O. *et al.* DMPK protein isoforms are differentially expressed in myogenic and neural cell lineages. *Muscle and Nerve* **40**, 545–555 (2009).
17. Gomes-Pereira, M. *et al.* CTG trinucleotide repeat ‘big jumps’: Large expansions, small mice. *PLoS Genet.* **3**, 0488–0491 (2007).
18. Huguet, A. *et al.* Molecular, Physiological, and Motor Performance Defects in DMSXL Mice Carrying >1,000 CTG Repeats from the Human DM1 Locus. *PLoS Genet.* **8**, e1003043 (2012).
19. Panaite, P. A., Kuntzer, T., Gourdon, G., Lobrinus, J. A. & Barakat-Walter, I. Functional and histopathological identification of the respiratory failure in a DMSXL transgenic mouse model of myotonic dystrophy. *DMM Dis. Model. Mech.* **6**, 622–631 (2013).
20. Gourdon, G. *et al.* The DMSXL transgenic mice carrying very large expansions exhibit molecular and physiological defects: an animal model for gene therapy experiments? *Medizinische Genet.* **21**, 409 (2009).

21. Algalarrondo, V. *et al.* Abnormal sodium current properties contribute to cardiac electrical and contractile dysfunction in a mouse model of myotonic dystrophy type 1. *Neuromuscul. Disord.* **25**, 308–320 (2015).
22. Sicot, G. *et al.* Downregulation of the Glial GLT1 Glutamate Transporter and Purkinje Cell Dysfunction in a Mouse Model of Myotonic Dystrophy. *Cell Rep.* **19**, 2718–2729 (2017).
23. Ghézali, G. *et al.* Connexin 30 controls astroglial polarization during postnatal brain development. *Development* **145**, dev155275 (2018).
24. Nixdorf-Bergweiler, B. E., Albrecht, D. & Heinemann, U. Developmental changes in the number, size, and orientation of GFAP-positive cells in the CA1 region of rat hippocampus. *Glia* **12**, 180–195 (1994).
25. Atienza, J. M., Zhu, J., Wang, X., Xu, X. & Abassi, Y. Dynamic monitoring of cell adhesion and spreading on microelectronic sensor arrays. *J. Biomol. Screen.* **10**, 795–805 (2005).
26. Braz, S. O., Dinca, D. M., Gourdon, G. & Gomes-Pereira, M. Real time videomicroscopy and semiautomated analysis of brain cell culture models of trinucleotide repeat expansion diseases. in *Methods in Molecular Biology* vol. 2056 217–240 (2020).
27. Seznec, H. *et al.* Transgenic mice carrying large human genomic sequences with expanded CTG repeat mimic closely the DM CTG repeat intergenerational and somatic instability. *Hum. Mol. Genet.* **9**, 1185–1194 (2000).
28. Burridge, K. Focal adhesions: a personal perspective on a half century of progress. *FEBS J.* **284**, 3355–3361 (2017).
29. Etienne-Manneville, S. In vitro assay of primary astrocyte migration as a tool to study Rho GTPase function in cell polarization. *Methods Enzymol.* **406**, 565–578 (2006).
30. Sergeant, N. *et al.* Dysregulation of human brain microtubule-associated tau mRNA maturation in myotonic dystrophy type 1. *Hum. Mol. Genet.* **10**, 2143–2155 (2001).
31. Venables, J. P. *et al.* MBNL1 and RBFOX2 cooperate to establish a splicing programme involved in pluripotent stem cell differentiation. *Nat. Commun.* **4**, 1–10 (2013).
32. Zhou, Z. *et al.* α 6-Integrin alternative splicing: Distinct cytoplasmic variants in stem cell fate specification and niche interaction. *Stem Cell Res. Ther.* **9**, 1–7 (2018).
33. Artero, R. *et al.* The muscleblind gene participates in the organization of Z-bands and epidermal attachments of *Drosophila* muscles and is regulated by Dmef2. *Dev. Biol.* **195**, 131–143 (1998).
34. Adereth, Y., Dammai, V., Kose, N., Li, R. & Hsu, T. RNA-dependent integrin α 3 protein localization regulated by the Muscleblind-like protein MLP1. *Nat. Cell Biol.* **7**, 1140–1147 (2005).

35. Wang, E. T. *et al.* Antagonistic regulation of mRNA expression and splicing by CELF and MBNL proteins. *Genome Res.* **25**, 858–871 (2015).
36. Park, Y. K. & Goda, Y. Integrins in synapse regulation. *Nat. Rev. Neurosci.* **17**, 745–756 (2016).
37. Cho, S., Muthukumar, A. K., Stork, T., Coutinho-Budd, J. C. & Freeman, M. R. Focal adhesion molecules regulate astrocyte morphology and glutamate transporters to suppress seizure-like behavior. *Proc. Natl. Acad. Sci. U. S. A.* **115**, 11316–11321 (2018).
38. Charizanis, K. *et al.* Muscleblind-like 2-Mediated Alternative Splicing in the Developing Brain and Dysregulation in Myotonic Dystrophy. *Neuron* **75**, 437–450 (2012).
39. Etienne-Manneville, S. Actin and microtubules in cell motility: Which one is in control? *Traffic* **5**, 470–477 (2004).
40. Miller, P. M. *et al.* Golgi-derived CLASP-dependent microtubules control Golgi organization and polarized trafficking in motile cells. *Nat. Cell Biol.* **11**, 1069–1080 (2009).
41. Zhang, M. *et al.* CAP interacts with cytoskeletal proteins and regulates adhesion-mediated ERK activation and motility. *EMBO J.* **25**, 5284–5293 (2006).
42. Orlofsky, A. Positioning of the centrosome and golgi complex. *Results Probl. Cell Differ.* **67**, 127–200 (2019).
43. Webb, D. J., Parsons, J. T. & Horwitz, A. F. Adhesion assembly, disassembly and turnover in migrating cells - Over and over and over again. *Nat. Cell Biol.* **4**, E97-100 (2002).
44. Guerrini, R. & Parrini, E. Neuronal migration disorders. *Neurobiol. Dis.* **38**, 154–166 (2010).
45. Khakh, B. S. & Deneen, B. The Emerging Nature of Astrocyte Diversity. *Annu. Rev. Neurosci.* **42**, 187–207 (2019).
46. Weigel, M., Wang, L. & Fu, M. meng. Microtubule organization and dynamics in oligodendrocytes, astrocytes, and microglia. *Dev. Neurobiol.* (2020) doi:10.1002/dneu.22753.
47. Preston, A. N., Cervasio, D. A. & Laughlin, S. T. Visualizing the brain 's astrocytes. **622**, 129–151 (2019).
48. Molofsky, A. V. *et al.* Astrocytes and disease: A neurodevelopmental perspective. *Genes Dev.* **26**, 891–907 (2012).
49. Dossi, E., Vasile, F. & Rouach, N. Human astrocytes in the diseased brain. *Brain Res. Bull.* **136**, 139–156 (2018).

50. Bushong, E. A., Martone, M. E. & Ellisman, M. H. Maturation of astrocyte morphology and the establishment of astrocyte domains during postnatal hippocampal development. *Int. J. Dev. Neurosci.* **22**, 73–86 (2004).
51. Zhou, B., Zuo, Y. X. & Jiang, R. T. Astrocyte morphology: Diversity, plasticity, and role in neurological diseases. *CNS Neurosci. Ther.* **25**, 665–673 (2019).
52. Wang, Q., Jie, W., Liu, J. H., Yang, J. M. & Gao, T. M. An astroglial basis of major depressive disorder? An overview. *Glia* **65**, 1227–1250 (2017).
53. Winblad, S., Lindberg, C. & Hansen, S. Temperament and character in patients with classical myotonic dystrophy type 1 (DM-1). *Neuromuscul. Disord.* **15**, 287–292 (2005).
54. Bruyère, J. *et al.* Heparan sulfate saccharides modify focal adhesions: Implication in mucopolysaccharidosis neuropathophysiology. *J. Mol. Biol.* **427**, 775–791 (2015).
55. Schindelin, J. *et al.* Fiji: An open-source platform for biological-image analysis. *Nat. Methods* **9**, 676–682 (2012).
56. Gorelik, R. & Gautreau, A. Quantitative and unbiased analysis of directional persistence in cell migration. *Nat. Protoc.* **9**, 1931–1943 (2014).
57. Lambert, M. P. *et al.* The RNA helicase DDX17 controls the transcriptional activity of REST and the expression of proneural microRNAs in neuronal differentiation. *Nucleic Acids Res.* **46**, 7686–7700 (2018).
58. Benoit-Pilven, C. *et al.* Complementarity of assembly-first and mapping-first approaches for alternative splicing annotation and differential analysis from RNAseq data. *Sci. Rep.* **8**, 4307 (2018).
59. Fontrodona, N. *et al.* Interplay between coding and exonic splicing regulatory sequences. *Genome Res.* **29**, 711–722 (2019).
60. Liao, Y., Wang, J., Jaehnig, E. J., Shi, Z. & Zhang, B. WebGestalt 2019: gene set analysis toolkit with revamped UIs and APIs. *Nucleic Acids Res.* **47**, W199–W205 (2019).
61. Pillet, L. E. *et al.* The intellectual disability protein Oligophrenin-1 controls astrocyte morphology and migration. *Glia* **68**, 1729–1742 (2020).
62. Abramoff, M. D., Magalhães, P. J. & Ram, S. J. Image processing with imageJ. *Biophotonics Int.* **11**, 36–41 (2004).

Declarations

Acknowledgements

We are grateful to the personnel of CERFE (Centre d'Exploration et de Recherche Fonctionnelle Expérimentale, Genopole, Evry, France) and LEAT (Laboratoire d'Expérimentation Animale, Imagine Institute, Paris, France) for attentively caring for the mice. We thank the Cell Imaging Platform of the Structure Fédérative de Recherche Necker for the useful help in microscopy acquisitions and analyses, and the support provided by the PSMN (Pôle Scientifique de Modélisation Numérique) of the ENS de Lyon for computing resources. This study was supported by grants from Agence Nationale de Recherche (ANR, France, Project Grant DM_Neuroglia to G.G., N.R., D.A. and C.M.), AFM-Téléthon (France, Project Grant 19920 to M.G.-P.), European Research Council (Consolidator Grant #683154 to N.R.), European Union's Horizon 2020 research and innovation program (Marie Skłodowska-Curie Innovative Training Networks, grant #722053, EU-GliaPhD to N.R.), CONACyT (Mexico, Project Grant CB-2012-01/183697 to O.H.H.), INSERM (France), Université Paris Descartes (France), as well as PhD fellowships from Ministère Français de la Recherche et Technologie (France, to D.M.D., G.S. and L.-E.P.), AFM-Téléthon (France, to D.M.D. and G.S.).

Author contributions

Conceptualization, D.M.D., C.M., D.A.; N.R., C.F.B., G.G., M.G.-P.; Methodology, D.M.D, G.S., S.O.B., C.M., O.H.-H., D.A., G.G., M.G.-P.; Validation, A.G.-B., S.O.B., L.L., J.T.; Formal Analysis, D.M.D., A.G.-B., L.-E.P., N.C., H.P., C.F.B., M.G.-P.; Investigation, D.M.D., A.G.-B., G.S., L.-E.P., N.C., S.O.B., L.L., A.H.L., C.N.A.-V., L.E.A.-J., J.T., M.G.-P.; Resources, O.H.-H., C.M., D.A., N.R., C.F.B., G.G., M.G.P.; Writing – Original draft, D.M.D, M.G.-P; Writing – Review & Editing, D.M.D., A.G.-B., C.M., D.A., N.R., C.F.B., G.G., M.G.-P.; Visualization, D.M.D., L.E.-P., N.C., O.H.-H., M.G.-P.; Supervision, D.A., N.R., C.F.B., G.G., M.G.-P.; Project Administration, M.G.-P; Funding Acquisition, C.M., D.A., N.R., C.F.B., G.G., M.G.-P. All authors read and approved the final manuscript.

Competing interests

The authors declare no competing interests.

Additional Information

Supplementary information is available for this paper.

Correspondence and requests for materials should be addressed to M.G.-P. and G.G.

Figures

Figure 1

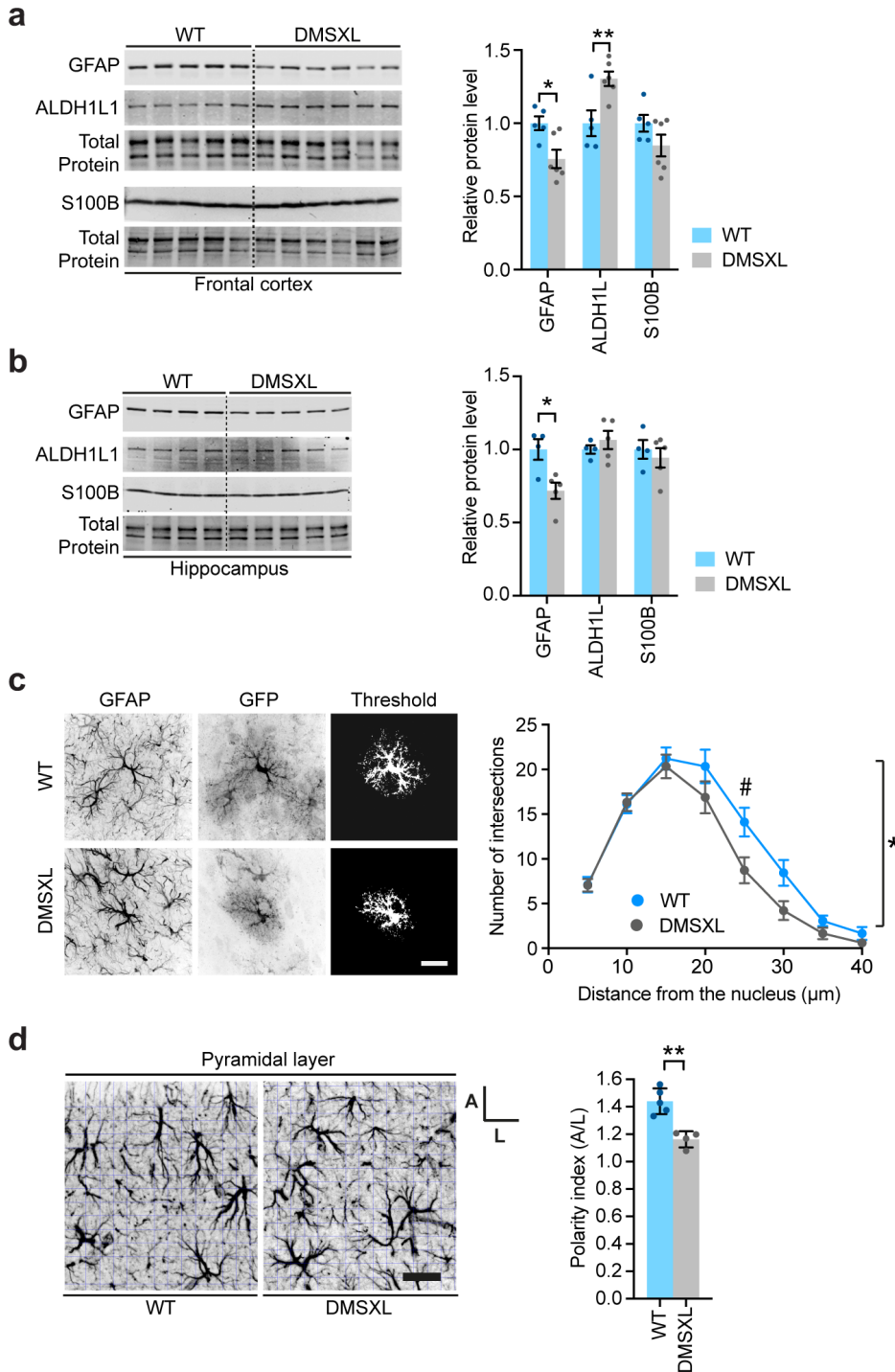


Figure 1

DMSXL astrocytes show abnormal morphology and polarity in vivo. (a) Western blot quantification of GFAP, ALDH1L1 and S100B in DMSXL frontal cortex at 1 month. Data are means \pm SEM. $n = 5$, WT; $n = 6$, DMSXL (* $p < 0.05$; ** $p < 0.01$; Two-way ANOVA, Sidak post-hoc test for multiple comparisons). (b) Western

blot quantification of GFAP, ALHD1L1 and S100B in the DMSXL hippocampus at 1 month of age. Data are means \pm SEM. n = 4, WT; n = 5, DMSXL (*p<0.05; Two-way ANOVA, Sidak post hoc test for multiple comparisons). (c) Sholl analysis of the branching of DMSXL cortical astrocytes. Representative pictures illustrating the specificity of the GFP labeling in astrocytes expressing the GFAP marker. GFP signal was analyzed by applying the same threshold to all images. Scale bar, 20 μ M. Data are means \pm SEM. N=5 mice, n=20 cells, WT; N=4 mice, n=20 cells, DMSXL (*p<0.05, Two-way repeats measures ANOVA; #p<0.05, Sidak post-hoc test for multiple comparisons). (d) Analysis of astrocyte polarity with respect to the pyramidal cell layer in 1-month-old mice. Schematic representation of grid-baseline analysis for orientation quantification of GFAP-labeled CA1 stratum radiatum astrocytes. Polarity index ratio (A/L) larger than one indicates preferential perpendicular orientation towards the pyramidal layer. Scale bar, 20 μ m. Data are means \pm SEM. N=4 mice, WT; N=5, DMSXL; n=8-16 cells studied per mouse (**p<0.01, Student's t test).

Figure 2

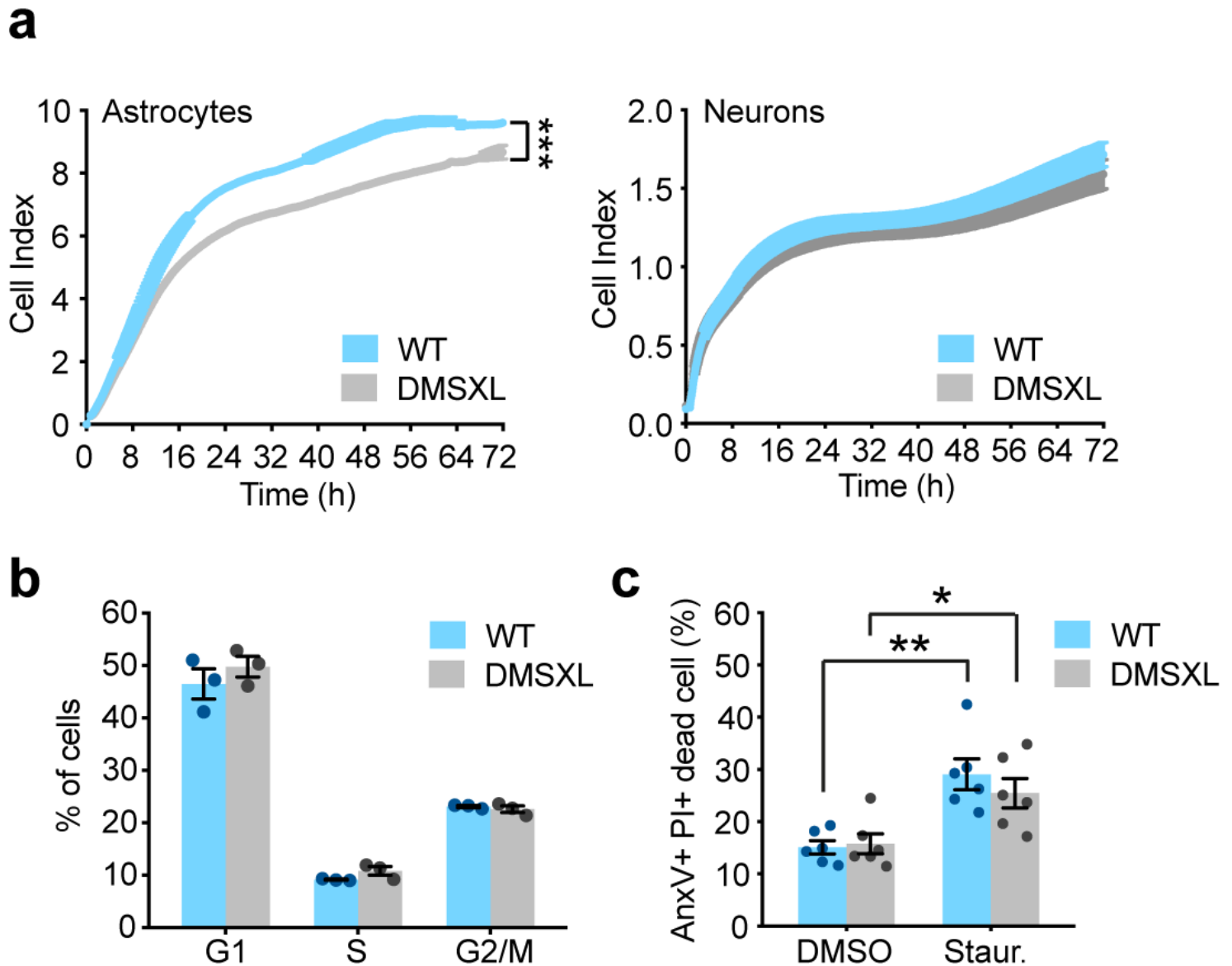


Figure 2

Primary DMSXL astrocytes display abnormal population dynamics. (a) xCELLigence cell index of primary astrocytes and primary neurons over 72 hours. Data are mean \pm SEM, $n=3-6$ independent cultures per group (** $p < 0.001$, Two-way repeated measures ANOVA). (b) Percentage of DMSXL and WT astrocytes in G1, S and G2/M phases of the cell cycle by FACS analysis of DNA content (PI levels) and DNA synthesis (BrdU incorporation). Data are mean \pm SEM, $n=3$ independent cultures per genotype. (c) FACS analysis of DMSXL and WT astrocyte cell death under control conditions (DMSO) and in the presence of Staurosporine (Staur). Percentage of apoptotic cells labeled with annexin V (AnxV+), and necrotic cells

labelled with propidium iodide (PI+). Data are mean \pm SEM, n=6 independent cultures per genotype (*p<0.05, **p<0.01, Two-way ANOVA and Sidak post-hoc test for multiple comparisons).

Figure 3

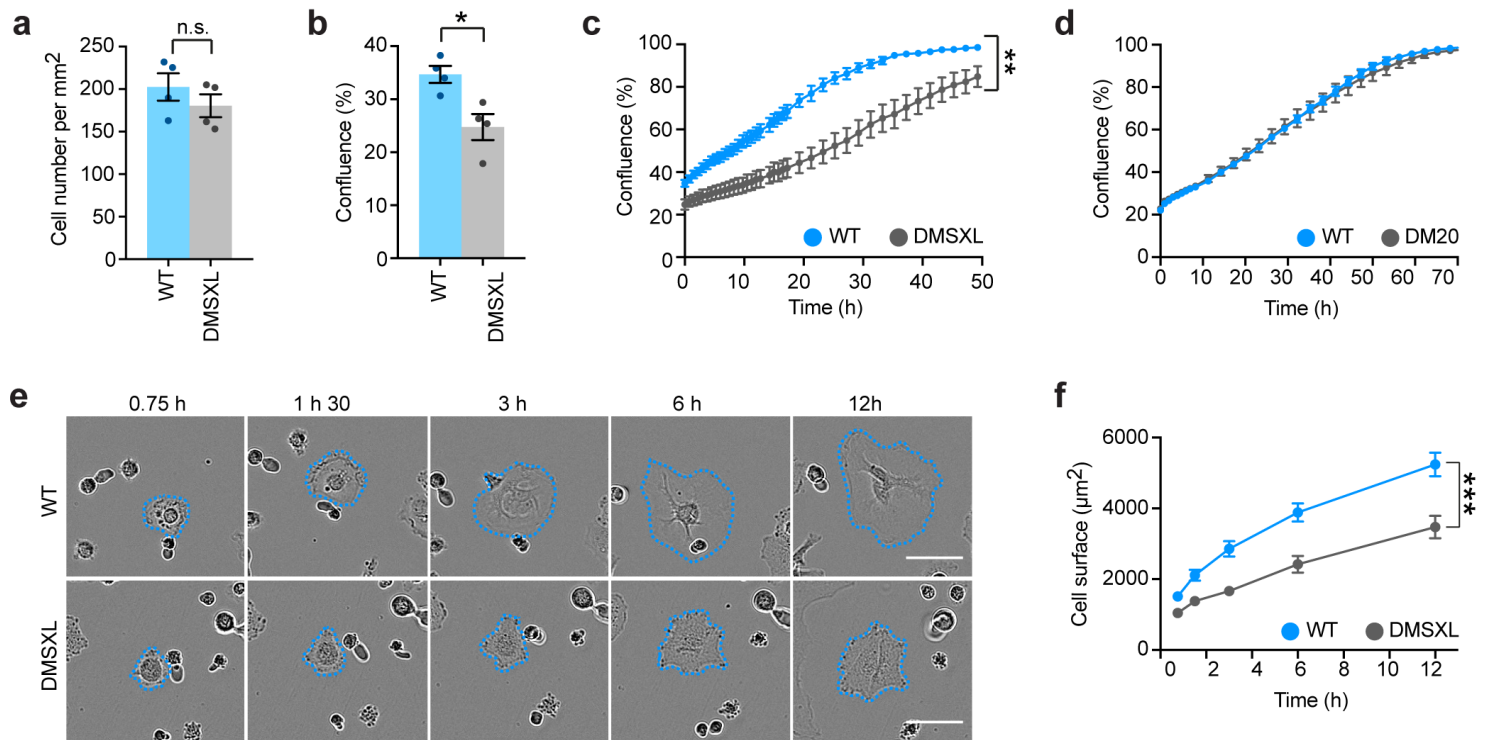


Figure 3

Primary DMSXL astrocytes exhibit abnormal adhesion and spreading. (a) Quantification of the number of DMSXL and WT astrocytes attached 45 minutes after plating. Data are means \pm SEM, n=4 independent cultures per genotype. n.s., not significant. (b) Semi-automated quantification of cell culture confluence 45 minutes after plating. Data are means \pm SEM, n=4 independent cultures per genotype (*p<0.05, Mann-Whitney U test). (c) Videomicroscopy semi-automated monitoring of DMSXL and WT astrocyte confluence, from 45 minutes after plating up to 48 hours in culture. Data are means \pm SEM, n=4 independent cultures per genotype (**p<0.001, Two-way repeated measures ANOVA). (d) Quantification of the confluence of DM20 and WT astrocyte cultures over time. Data are means \pm SEM, n=3 independent cultures per genotype. (e) Representative time-lapse bright field images of primary DMSXL and WT astrocytes, over 12 hours after plating. Scale bar, 50 μ m. (f) Quantification of the surface of individual primary astrocytes over time (n = 72, WT; n=64, DMSXL). Data are means \pm SEM (***p<0.001, Two-way repeated measures ANOVA).

Figure 4

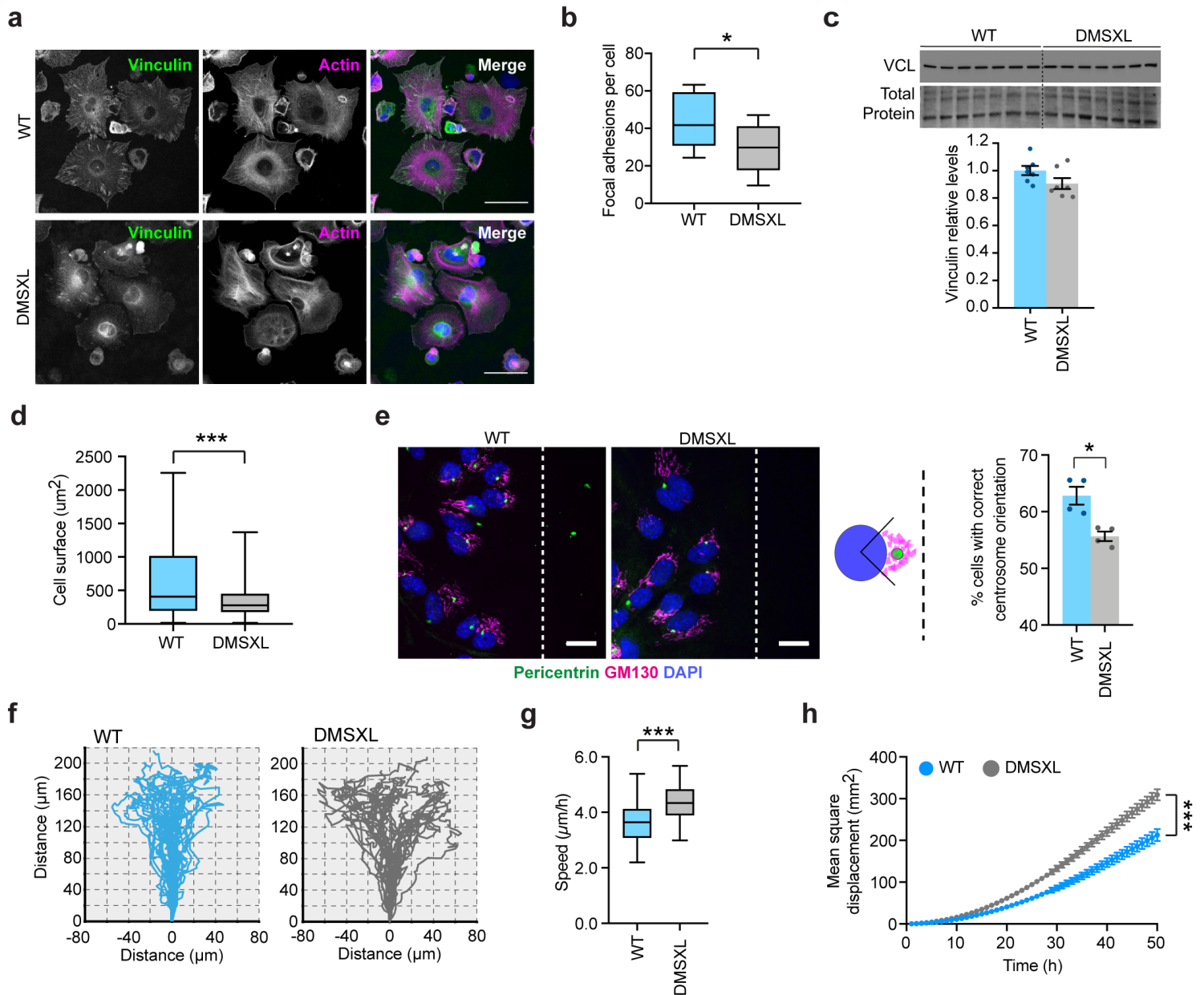


Figure 4

DMSXL astrocytes show defects in focal adhesion organization, cytoskeleton reorientation and cell migration. (a) Immunofluorescence of vinculin-rich focal adhesions and staining of actin cytoskeleton with phalloidin in DMSXL and WT astrocytes, following 3 h in culture. Scale bar, 50 μm . (b) Quantification of focal adhesions, assessed by the number of vinculin-rich clusters. Tukey whisker plots represent the number of focal adhesions per cell. N=2 independent cultures per genotype; n=609, DMSXL; n=538, WT (* p <0.05, Student's t test). (c) Western blot quantification of vinculin expression in primary DMSXL and WT astrocytes. Data are means \pm SEM; n=7 independent cultures per genotype. (d) Measurement of actin cytoskeleton spreading. Data are shown as Tukey whisker plots. N=2 independent cultures per genotype; n=487 cells, DMSXL; n=440 cells, WT (** p <0.001, Mann-Whitney U test). (e) Analysis of MTOC and Golgi

apparatus orientation through the immunofluorescent labeling of pericentrin and GM130, respectively, 8 h after wound-induced migration. Scale bar, 20 μm . Quantification of the percentage of cells with centrosome and Golgi orientated perpendicularly to wound. Data are means \pm SEM. N=4 independent cultures per genotype; n=2179 cells, WT; n=2068 cells, DMSXL (* p <0.05, Student t test). (f) Representative migration tracking plots of individual DMSXL and WT astrocytes over 50 h, until complete wound closure. (g) Average cell speed of primary astrocytes during migration. Data are represented in Tukey whisker plot. N=2 independent cultures per genotype; n=39 cells, WT; n=39 cells, DMSXL (** p <0.001, Student's t test). (h) Mean square displacement of primary astrocytes in culture over 50 hours of cell migration, until complete wound closure. Data are means \pm SEM. N=2 independent cultures per genotype; n=39 cells, WT; n=39 cells, DMSXL (** p <0.001, Two-way ANOVA).

Figure 5

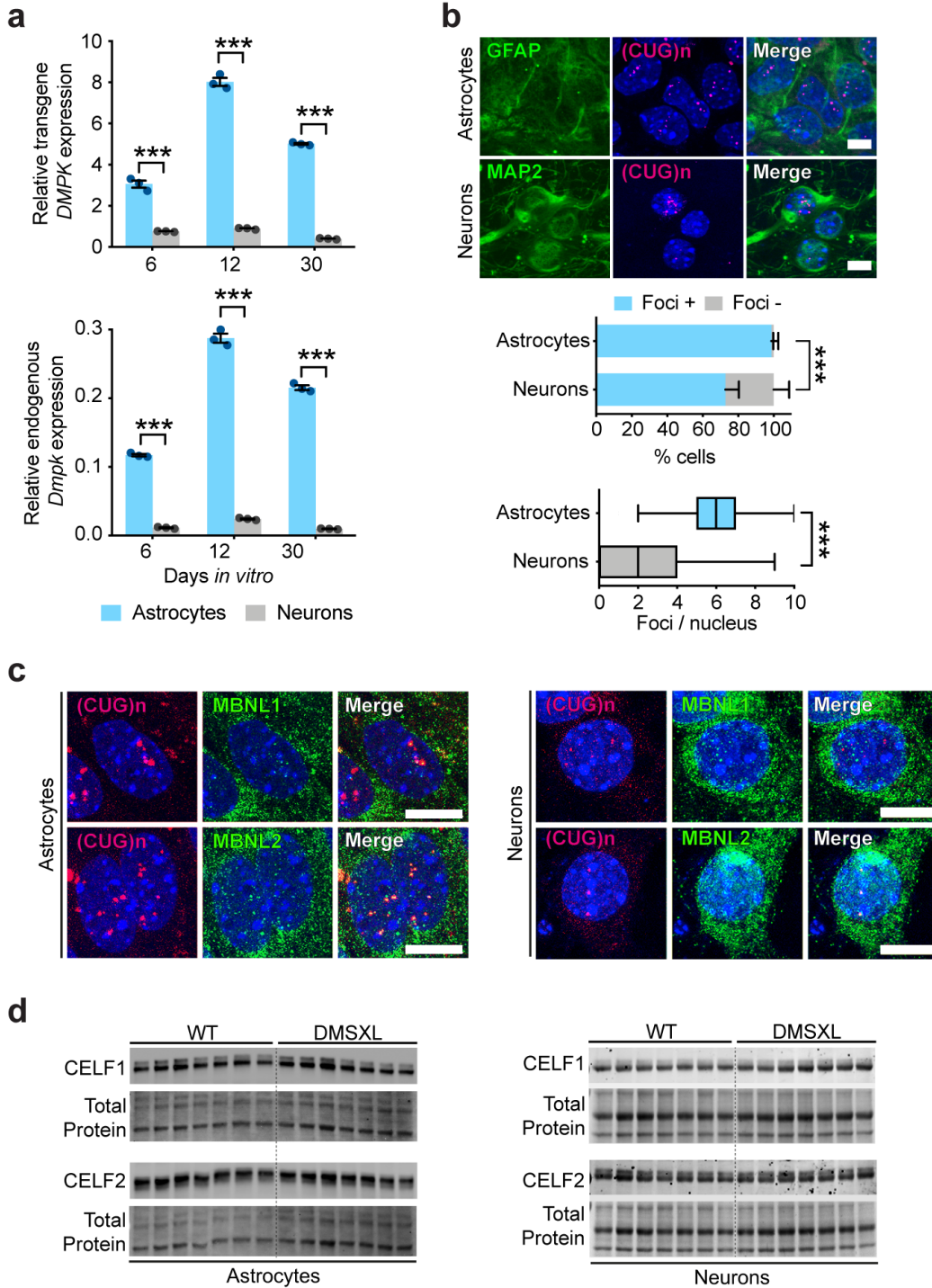


Figure 5

DM1 RNA toxicity is more pronounced in mouse astrocytes than in neurons. (a) Expression of human DMPK transgene and mouse endogenous Dmpk relative to 18S rRNA internal control in primary DMSXL astrocytes and neurons at 6, 12 and 30 days in vitro. Data are means \pm SEM, $n=3$ independent cultures per group ($***p<0.001$, Two-way ANOVA, Sidak post-hoc pair-wise comparisons). (b) FISH analysis of nuclear foci accumulation in primary DMSXL astrocytes and neurons. Percentage of GFAP-expressing

astrocytes and MAP-expressing neurons containing foci (** $p < 0.001$, χ^2 test). Data are means \pm SEM. Tukey whisker plots representing the number of foci per nucleus in primary DMSXL astrocytes and neurons (** $p < 0.001$, Mann-Whitney U test). $N = 3$ independent cultures per cell type; $n = 166$, astrocytes, $n = 125$ neurons Scale bar, 10 μm . (c) FISH of RNA foci (magenta) combined with IF detection of MBNL1 and MBNL2 (green) in primary astrocytes and neurons of DMSXL mice. Scale bar, 10 μm . Nuclei are stained with DAPI (blue). (d) Western blot detection of CELF1 and CELF2 in primary astrocytes and neurons from DMSXL and WT mice.

Figure 6

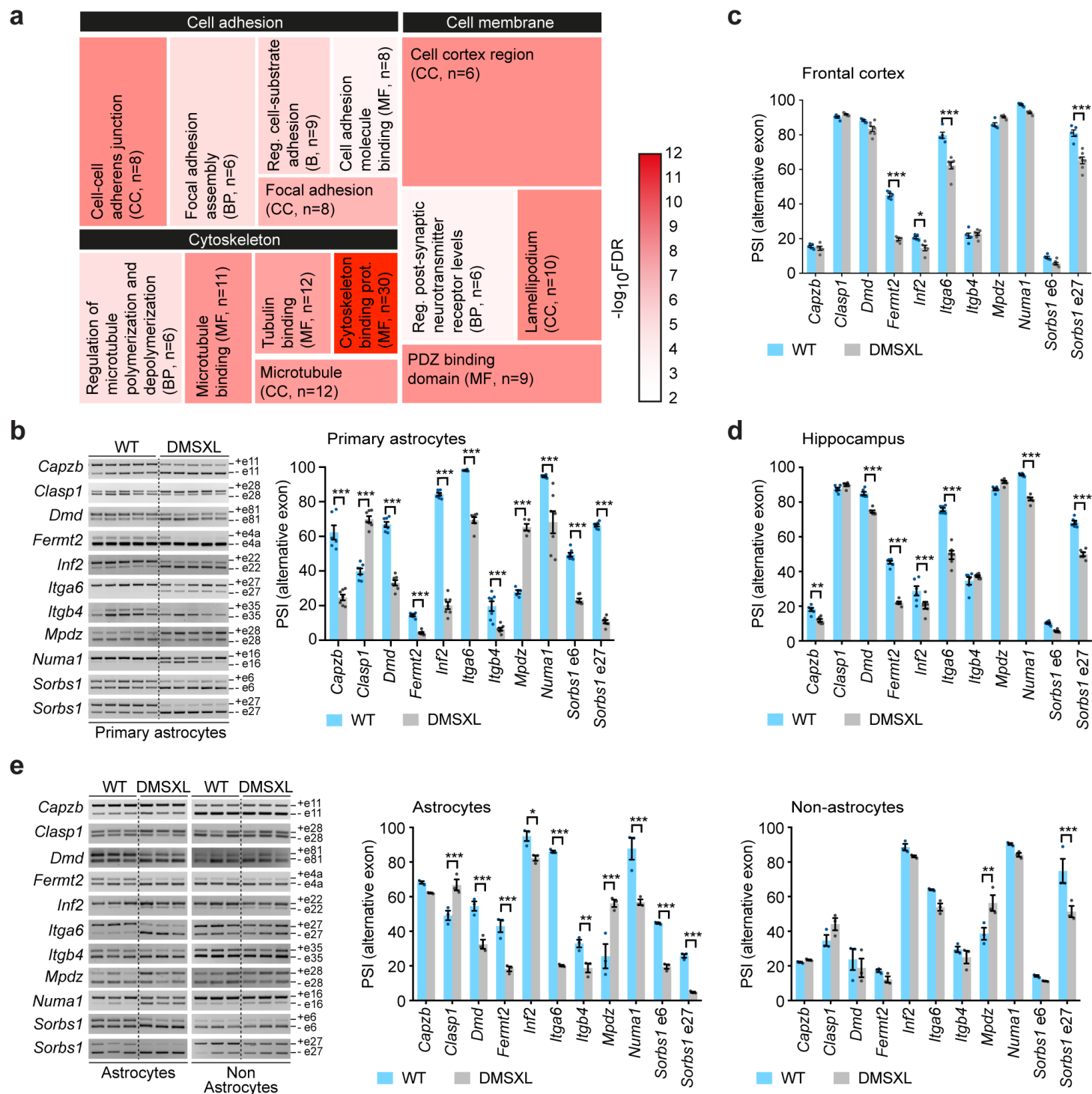


Figure 6

RNA sequencing of primary DMSXL astrocytes indicates defects in cell adhesion, cytoskeleton and cell membrane. (a) Tree map representation of enriched non-redundant GO terms associated with the abnormally spliced genes in primary DMSXL astrocytes, and distributed by three main categories. Cell sizes are proportional to the enrichment ratio of each GO term. The heatmap scale represents the $-\log_{10}(\text{FDR})$ of enrichment. BP, biological process. CC, cellular component. MF, molecular function. The number of misspliced genes (n) in each category is shown. (b) Representative RT-PCR splicing analysis of selected transcripts that regulate cell adhesion and cytoskeleton in primary DMSXL and WT astrocytes. Alternative exons are indicated on the right. The graph represents the PSI of alternative exons. Data are means \pm SEM, n=5-7 independent cultures per genotype (***p<0.001; Two-way ANOVA, Sidak post-hoc test for multiple comparisons). (c) Splicing dysregulation of adhesion- and cytoskeleton-associated transcripts in DMSXL frontal cortex. Data are means \pm SEM, n=5-7 mice per genotype (*p<0.05; ***p<0.001; Two-way ANOVA, Sidak post-hoc test for multiple comparisons). (d) Splicing dysregulation of adhesion- and cytoskeleton-associated transcripts in DMSXL hippocampus. Data are means \pm SEM, n=6 mice per genotype (*p<0.05; ***p<0.001; Two-way ANOVA, Sidak post-hoc test for multiple comparisons). (e) Representative RT-PCR splicing analysis in cortical astrocytes and non-astrocyte cells isolated from 1-month-old mice. PSI of alternative exons in astrocytes and non-astrocyte cell fractions. Data are means \pm SEM, n=3 mice per genotype (*p<0.05; **p<0.01; ***p<0.001; Two-way ANOVA, Sidak post-hoc test for multiple comparisons).

Figure 7

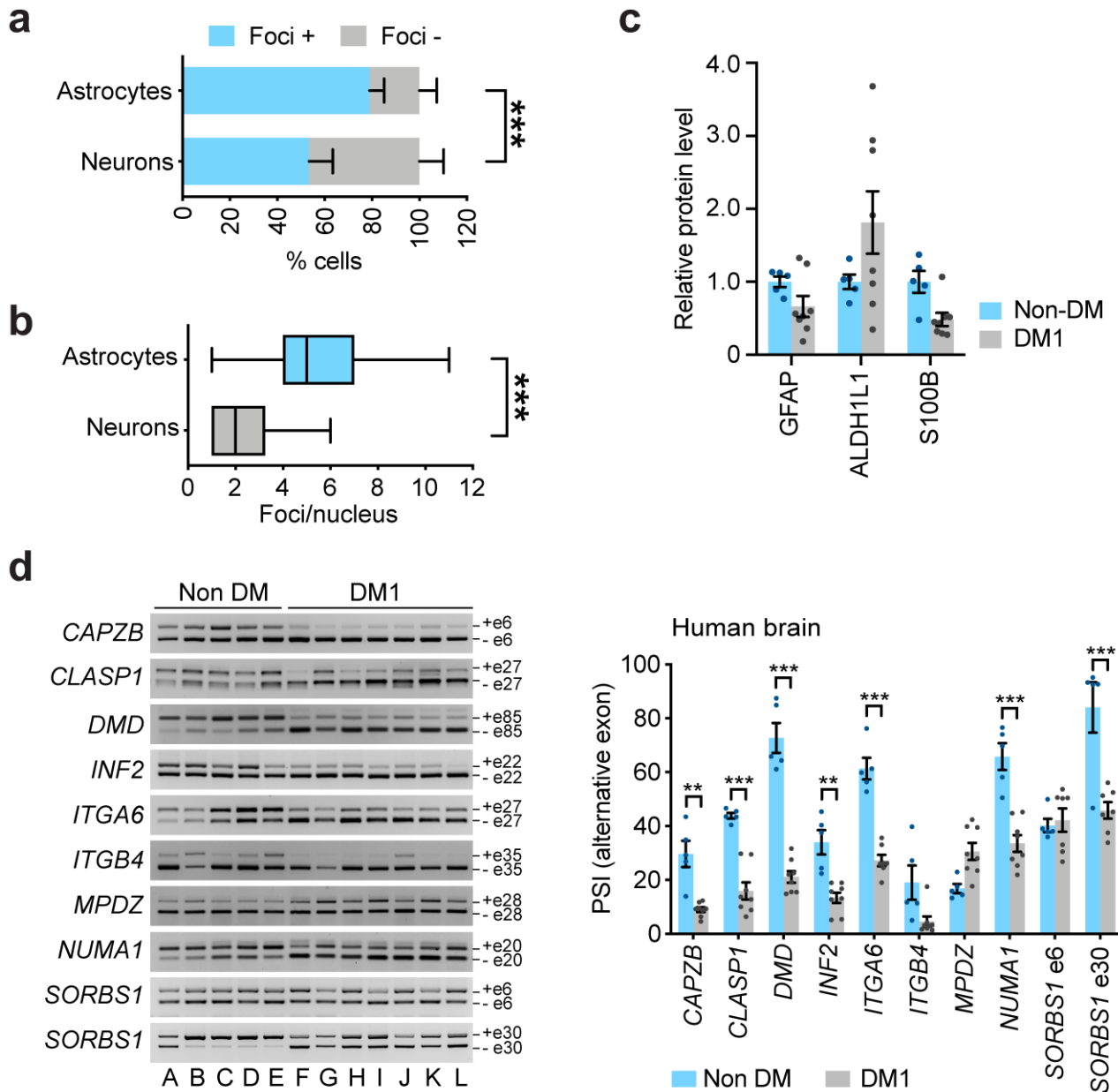


Figure 7

Pronounced foci accumulation in astrocytes and splicing dysregulation of adhesion and cytoskeleton-related transcripts in human DM1 brains. (a) Percentage of GFAP-positive astrocytes and MAP-positive neurons exhibiting nuclear RNA foci in the frontal cortex of DM1 patients ($***p < 0.001$, χ^2 test). Data are means \pm SEM, $n=3$. (b) Tukey whisker plots representing the number of foci per nucleus in human cortical astrocytes and neurons ($***p < 0.001$, Mann-Whitney U test). $N=3$ DM1 patients; $n=284$, astrocytes; $n=202$,

neurons. (c) Western blot quantification of GFAP, ALHD1L1 and S100B astrocyte proteins in human frontal cortex. Data are means \pm SEM. n=5, non-DM; n=8, DM1. (d) RT-PCR splicing of adhesion- and cytoskeleton-associated transcripts in the frontal cortex of adult DM1 patients and non-DM subjects. Alternative exons are indicated on the right. Quantification of PSI of alternative exons. Data are means \pm SEM. n=5, non-DM; n=7, DM1 (**p<0.01; ***p<0.001; Two-way ANOVA, Sidak post hoc test for multiple comparisons).

Supplementary Files

This is a list of supplementary files associated with this preprint. Click to download.

- [NCOMMS2051264ReportingSummary.pdf](#)
- [DincaSupplementaryInformation.docx](#)